

Inflight magnetic characterization of the test masses onboard LISA Pathfinder

Marc Diaz-Aguiló^{1,2*} and Enrique García-Berro^{1,2}

¹*Departament de Física Aplicada, Universitat Politècnica de Catalunya,
c/Esteve Terrades, 5, 08860 Castelldefels, Spain*

²*Institut d'Estudis Espacials de Catalunya, c/Gran Capità 2-4, Edif. Nexus 104, 08034 Barcelona, Spain*

Alberto Lobo^{3,2}

³*Institut de Ciències de l'Espai, CSIC, Campus UAB,
Facultat de Ciències, Torre C-5, 08193 Bellaterra, Spain*

(Dated: October 30, 2018)

LISA Pathfinder is a science and technology demonstrator of the European Space Agency within the framework of its LISA mission, the latter aiming to be the first space-borne gravitational wave observatory. The payload of LISA Pathfinder is the so-called LISA Technology Package, which is designed to measure relative accelerations between two test masses in nominal free fall. The diagnostics subsystem consists of several modules, one of which is the magnetic diagnostics unit. Its main function is the assessment of the differential acceleration noise between the test masses due to magnetic effects. This subsystem is composed of two onboard coils intended to produce controlled magnetic fields at the location of the test masses. These magnetic fields couple with the remanent magnetic moment and susceptibility and produce forces and torques on the test masses. These, in turn, produce kinematic excursions of the test masses which are sensed by the onboard interferometer. We prove that adequately processing these excursions, the magnetic properties of the test masses can be estimated using classical multi-parameter estimation techniques. Moreover, we show that special processing procedures to minimize the effect of the multi channel cross-talks are needed. Finally, we demonstrate that the quality of our estimates is frequency dependent. We also suggest that using a multiple frequency experiment the global estimate can be obtained in such a way that the results of the magnetic experiment are more reliable. Finally, using our procedure we compute the contribution of the magnetic noise to the total proof-mass acceleration noise.

PACS numbers: 04.80.Nn, 04.30.-w, 07.87.+v, 06.30.Ka, 07.05.Fb

I. INTRODUCTION

LISA Pathfinder (LPF) is a science and technology demonstrator programmed by the European Space Agency (ESA) within its LISA mission activities [1]. LISA (Laser Interferometer Space Antenna) is a joint ESA-NASA mission which will be the first low frequency (milli-Hz) gravitational wave detector, and also the first space-borne gravitational wave observatory. The payload of LPF, the LISA Technology Package (LTP), will be the highest sensitivity geodesic explorer flown to date. The LTP is designed to measure relative accelerations between two test masses in nominal free fall (geodesic motion) with a differential acceleration noise budget

$$S_{\delta a, LPF}^{1/2}(\omega) \leq 3 \times 10^{-14} \left[1 + \left(\frac{\omega/2\pi}{3 \text{ mHz}} \right)^2 \right] \frac{\text{m s}^{-2}}{\sqrt{\text{Hz}}} \quad (1)$$

in the frequency band between 1 mHz and 30 mHz [2, 3].

Magnetic noise in the LTP is allowed to be a significant fraction of the total mission acceleration noise: up to $1.2 \times 10^{-14} \text{ m s}^{-2} \text{ Hz}^{-1/2}$ is apportioned to magnetic effects, i.e., 40 % of the total noise, $3 \times 10^{-14} \text{ m s}^{-2} \text{ Hz}^{-1/2}$,

see Eq. (1). This noise occurs because the residual magnetization and susceptibility of the test masses couple to the surrounding magnetic field, giving rise to a fluctuating force which is given by:

$$\delta \mathbf{F} = \left\langle \left[\left(\mathbf{M} + \frac{\chi}{\mu_0} \mathbf{B} \right) \cdot \delta \nabla \right] \mathbf{B} + \frac{\chi}{\mu_0} [\delta \mathbf{B} \cdot \nabla] \mathbf{B} \right\rangle V \quad (2)$$

in each of the test masses. In this expression \mathbf{B} is the magnetic field in the test mass, χ and \mathbf{M} are its magnetic susceptibility and residual density of magnetic moment, respectively, and V is the volume of the test mass, μ_0 is the vacuum magnetic constant, $4\pi \times 10^{-7} \text{ m kg s}^{-2} \text{ A}^{-2}$, and $\langle \dots \rangle$ indicates test mass volume average of the enclosed quantity. Finally, $\delta \mathbf{B}$ represents the fluctuation of the magnetic field, and $\delta \nabla$ stands for the fluctuation of the gradient [4]. Quantitative assessment of the magnetic noise in the LTP, i.e. evaluation of Eq. (2) clearly requires a real-time monitoring of the magnetic field and an accurate knowledge of the magnetic characteristics of the test masses.

The determination of the magnetic characteristics of the test masses (remanent magnetic moment and susceptibility) must be done in flight because their magnetic properties may change due to launch stresses and other circumstances. This will be done injecting controlled sinusoidal magnetic fields at the positions of the test masses and appropriately processing the resulting kinematics, which will be obtained from the readings de-

*marc.diaz.aguilo@fa.upc.edu

livered by the onboard interferometer. Although the basic design of the magnetic experiment is well settled [5], due to the high complexity of the LTP experiment, more in-depth analyses based on a more realistic modeling are necessary to assess its feasibility and performance. The purpose of this paper is, precisely, to fill this gap. In particular, we model in a realistic way the kinematics of the test masses and we evaluate the expected quality of the estimates of the magnetic moment and susceptibility. Specifically, we take into account several effects — like the cross-talks between some of the channels of the instrument, or the frequency-dependent parameters of the control loops governing the dynamics of the test masses — that previous analyses disregarded. All these effects depend on the frequency used to excite the test masses. Hence, the quality of the estimates of the magnetic data depends sensitively on the excitation frequency, since the satellite does not behave equally across the complete measurement bandwidth. Therefore, it is important to determine the quality of the estimates across the complete measurement bandwidth, and the frequencies that deliver the best estimate of the magnetic parameters.

The paper is organized as follows. In Sect. II we give a brief description of the magnetic experiment intended to estimate the magnetic properties of the test masses. Then, in Sect. III we briefly present the dynamical model of the satellite. It follows Sect. IV, where we discuss the estimation model and the estimation procedures used in this work. In Sect. V we present the sensitivity of this model to different hardware systems of the satellite and in Sect. VI we evaluate the frequency dependence of the experiment, and we optimize its performance with respect to the excitation frequency. Sect. VII is devoted to analyze the robustness of our results. Sect. VIII determines the expected accuracy of the magnetic contribution to the total proof-mass acceleration noise. Finally, in Sect. IX we summarize our main findings, we discuss the significance of our results, and we draw our conclusions.

II. EXPERIMENT OVERVIEW

The two test masses are located at the center of each inertial sensor — the two towers in Fig. 1 — and are the end mirrors of the Optical Metrology System, that senses the positions and attitudes of the test masses. The optical bench of the interferometer can be seen in Fig. 1 as well. In fact, one of the test masses is the reference free floating body to perform the translation and attitude control of the spacecraft. The x -axis of the experiment is the axis connecting the two test masses centers, and it goes from test mass 1 to test mass 2. The z -axis points towards the solar panel (parallel to the two inertial sensor towers and upwards in Fig. 1) and, finally, the y -axis closes the right-handed Cartesian coordinate system. The test masses are made of an alloy of Pt (27%) and Au (73%), their dimensions are $46 \times 46 \times 46$ mm and

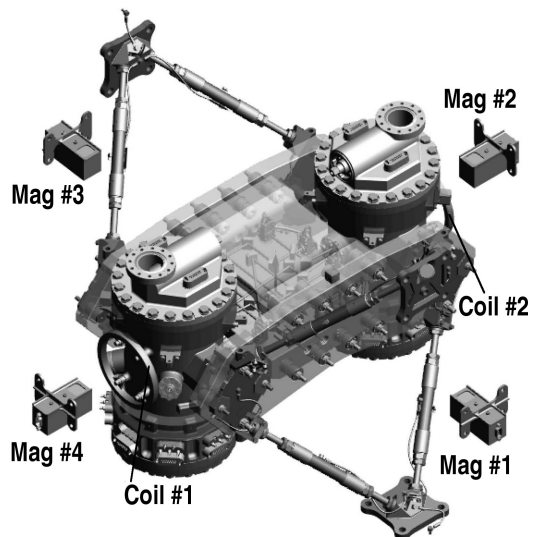


FIG. 1: A schematic view of the payload of LISA Pathfinder, the LTP. The Inertial Sensors (two vertical towers) host the two test masses. The four floating boxes correspond to the tri-axial fluxgate magnetometers, and the two induction coils are placed next to each of the test masses. The optical bench of the interferometer is located on the horizontal plane between the Inertial Sensors.

their weight is 1.95 kg. To comply with the top science requirements, the test masses must have certain properties. For the purpose of the present work the two most important properties are the remanent magnetic moment and the susceptibility. The remanent magnetic moment must be $|\mathbf{m}| < 2.0 \times 10^{-8}$ A m². Since the volume of the test masses is $V = 0.046^3$ m³, the density of magnetic moment must be then $|\mathbf{M}| < 9.451 \cdot 10^{-4}$ A/m. The susceptibility of the test mass can be suitably represented by a complex number, $\chi = \chi_o + i\chi_e$, where χ_o is its real component and $\chi_e(\omega)$ is a frequency-dependent imaginary term which is due to the eddy currents on the test mass [2, 3]. The requirement on the value of the real component is $\chi_o < 2.5 \times 10^{-5}$.

As mentioned, to measure the remanent magnetic moment and the susceptibility of the test masses a controlled magnetic field will be injected at the position of the test masses. This magnetic field produces forces and torques which excite the kinematics of the test masses. Studying the motion of the test masses, namely their displacement and rotation, allows to estimate the three components of the magnetic moment and the susceptibilities of the test masses.

A. The injected magnetic fields

The magnetic field at the position of the test masses will be generated by the injection of sinusoidal currents to the onboard coils. These onboard coils are placed next to each of the inertial sensors towers, see again Fig. 1.

The two circular induction coils are made of a titanium alloy ($\text{Ti}_6\text{Al}_4\text{V}$), and have $N = 2400$ windings of radius $r = 56.5$ mm [3]. They are placed 85.5 mm away from the center of the respective test mass. The onboard coils are aligned with the x -axis of the test masses, thus, the magnetic field within the volume of the test masses has axial symmetry. Given a current fed to the coils $I(t) = I_0 \sin \omega_0 t$, the resulting magnetic field (and its gradient) will oscillate at the same frequency. Therefore we write,

$$\mathbf{B}_{\text{app}} = \text{Re} \left\{ \mathbf{B}_0 i e^{-i\omega_0 t} \right\} = \mathbf{B}_0 \sin \omega_0 t \quad (3)$$

$$\nabla \mathbf{B}_{\text{app}} = \text{Re} \left\{ \nabla \mathbf{B}_0 i e^{-i\omega_0 t} \right\} = \nabla \mathbf{B}_0 \sin \omega_0 t \quad (4)$$

The field produced by the coils at the center of the test mass is $4.47 \mu\text{T}$, whereas the maximum environmental magnetic field expected during science operation is less than 100 nT. On the other hand, the magnetic field gradient along the x -axis produced by the coils is $109.2 \mu\text{T/m}$, while the maximum magnetic field gradient required by the mission science specification is $-5 \mu\text{T/m}$. Therefore, it is a safe assumption to neglect the effects of the environmental magnetic field with respect to the applied field by the coils. Thus, the forces and torques exerted on the test masses are computed as [6]:

$$\mathbf{F} = \left\langle \left[\left(\mathbf{M} + \text{Re} \left\{ \frac{\chi_o + i\chi_e}{\mu_0} \mathbf{B}_0 i e^{-i\omega_0 t} \right\} \right) \cdot \nabla \right] \mathbf{B}_{\text{app}} \right\rangle V \quad (5)$$

and

$$\begin{aligned} \mathbf{N} = & \left\langle \mathbf{M} \times \mathbf{B}_{\text{app}} + \mathbf{r} \times \left(\left[\mathbf{M} \cdot \nabla \right] \mathbf{B}_{\text{app}} \right. \right. \\ & \left. \left. + \left[\text{Re} \left\{ \frac{\chi_o + i\chi_e}{\mu_0} \mathbf{B}_0 i e^{-i\omega_0 t} \right\} \cdot \nabla \right] \mathbf{B}_{\text{app}} \right) \right\rangle V \quad (6) \end{aligned}$$

where \mathbf{B}_{app} is the field produced by the coils, and \mathbf{r} is the position vector that has the test mass center as origin. The term $\text{Re} \left\{ \frac{\chi_o + i\chi_e}{\mu_0} \mathbf{B}_0 i e^{-i\omega_0 t} \right\}$ is the induced magnetization by the externally applied field. Note that the forces and torques depend on \mathbf{M} , χ_o and χ_e .

Considering Eqs. (3), (4) and (5), the x -component of the force acting on the test mass is

$$\begin{aligned} F_x = & \frac{\chi_o V}{2\mu_0} \langle \mathbf{B}_0 \cdot \nabla B_{0,x} \rangle \\ & + \langle \mathbf{M} \cdot \nabla B_{0,x} \rangle V \sin \omega_0 t \\ & - \frac{\chi_o V}{2\mu_0} \langle \mathbf{B}_0 \cdot \nabla B_{0,x} \rangle \cos 2\omega_0 t \\ & - \frac{\chi_e V}{2\mu_0} \langle \mathbf{B}_0 \cdot \nabla B_{0,x} \rangle \cos(2\omega_0 t - \pi/2) \quad (7) \end{aligned}$$

where we have used that $\sin^2 \omega_0 t = (1 - \cos 2\omega_0 t)/2$ and the $\pi/2$ rad phase due to the complex component of the susceptibility has been added as an argument in the corresponding \cos term. As can be seen from this equation, the linear acceleration of the test masses along the x -axis

has two separate frequencies, one at ω_0 and the other at $2\omega_0$, and also a DC component. The $2\omega_0$ component presents an in-phase component proportional to χ_o and a quadrature component proportional to χ_e . Particularly, the ω_0 component can be more explicitly written as:

$$\langle \mathbf{M} \cdot \nabla B_{0,x} \rangle = \left\langle M_x \frac{\partial B_{0,x}}{\partial x} + M_y \frac{\partial B_{0,x}}{\partial y} + M_z \frac{\partial B_{0,x}}{\partial z} \right\rangle \quad (8)$$

where M_x , M_y , M_z are the components of the density of the remanent magnetic moment. If the test mass is homogeneous we have the simplified expression

$$\langle \mathbf{M} \cdot \nabla B_{0,x} \rangle = \left\langle M_x \frac{\partial B_{0,x}}{\partial x} \right\rangle \quad (9)$$

since the y and z components of $\nabla B_{0,x}$ average to zero due to symmetry of the field of the coil. This leads to a force component along the x -axis that only depends on M_x , χ_o and χ_e .

On the other hand, the torque acting on the test mass also has a similar behavior:

$$\begin{aligned} \mathbf{N} = & \langle \mathbf{M} \times \mathbf{B}_0 + \mathbf{r} \times \left[\left(\mathbf{M} \cdot \nabla \right) \mathbf{B}_0 \right] \rangle V \sin \omega_0 t \quad (10) \\ & + \left\langle \mathbf{r} \times \frac{\chi_o}{\mu_0} \left[\mathbf{B}_0 \cdot \nabla \right] \mathbf{B}_0 \right\rangle V \sin^2 \omega_0 t \\ & - \left\langle \mathbf{r} \times \frac{\chi_e}{\mu_0} \left[\mathbf{B}_0 \cdot \nabla \right] \mathbf{B}_0 \right\rangle V \sin \omega_0 t \cos \omega_0 t \end{aligned}$$

In this case, it must be noted that, because of the symmetry of the applied magnetic field, the terms multiplying $\sin^2 \omega_0 t$ and $\sin \omega_0 t \cos \omega_0 t$ in Eq. (10) vanish. The two rotation excursions detected by the interferometer using wavefront sensing are the rotations about the y -axis and z -axis. The magnitude of the rotation about the x -axis is smaller, and cannot be detected by the interferometer because the axis of rotation is aligned with the laser beam. Taking this into account, the two relevant torques for the experiment are:

$$\begin{aligned} N_y = & \left\langle M_z B_{0,x} - M_x B_{0,z} \right. \\ & \left. + z \left(\mathbf{M} \cdot \nabla B_{0,x} \right) \right. \\ & \left. - x \left(\mathbf{M} \cdot \nabla B_{0,z} \right) \right\rangle V \sin \omega_0 t \quad (11) \end{aligned}$$

$$\begin{aligned} N_z = & \left\langle M_x B_{0,y} - M_y B_{0,x} \right. \\ & \left. + x \left(\mathbf{M} \cdot \nabla B_{0,y} \right) \right. \\ & \left. - y \left(\mathbf{M} \cdot \nabla B_{0,x} \right) \right\rangle V \sin \omega_0 t \quad (12) \end{aligned}$$

These equations can be further simplified in the case of a homogeneous test mass. In this case, due to the axial symmetry of the magnetic field, the terms $\langle B_{0,z} \rangle$ in Eq. (11) and $\langle B_{0,y} \rangle$ in Eq. (12) vanish. Moreover, for the same reason the terms

$$\left\langle z \frac{\partial B_{0,x}}{\partial x} \right\rangle, \quad \left\langle z \frac{\partial B_{0,x}}{\partial y} \right\rangle,$$

and

$$\left\langle x \frac{\partial B_{0,z}}{\partial x} \right\rangle, \quad \left\langle x \frac{\partial B_{0,z}}{\partial y} \right\rangle$$

in Eq. (11) also vanish, as do the terms

$$\left\langle x \frac{\partial B_{0,y}}{\partial x} \right\rangle, \quad \left\langle x \frac{\partial B_{0,y}}{\partial z} \right\rangle,$$

$$\left\langle y \frac{\partial B_{0,x}}{\partial x} \right\rangle, \quad \left\langle y \frac{\partial B_{0,x}}{\partial z} \right\rangle$$

in Eq. (12). In these terms x , y and z are the three components of \mathbf{r} . Hence, the torque about the y -axis only depends on M_z and the torque about the z -axis only depends on M_y :

$$N_y = M_z \left\langle B_{0,x} + z \frac{\partial B_{0,x}}{\partial z} - x \frac{\partial B_{0,z}}{\partial z} \right\rangle V \sin \omega_0 t \quad (13)$$

$$N_z = M_y \left\langle -B_{0,x} + x \frac{\partial B_{0,y}}{\partial y} - y \frac{\partial B_{0,x}}{\partial y} \right\rangle V \sin \omega_0 t \quad (14)$$

Finally, we can cast Eqs. (7), (13) and (14) in the form:

$$\begin{aligned} F_x &= \chi_o f_{x_{DC}} + M_x f_{x_{1\omega_0}} + \chi_o f_{x_{2\omega}} + \chi_e f_{x_{2\omega_0}}'' \\ N_y &= M_z n_{y_{1\omega_0}} \\ N_z &= M_y n_{z_{1\omega_0}} \end{aligned} \quad (15)$$

where $f_{x_{DC}}$ is a constant function, $f_{x_{1\omega_0}}$, $n_{y_{1\omega_0}}$ and $n_{z_{1\omega_0}}$ oscillate at ω_0 and $f_{x_{2\omega}}$ and $f_{x_{2\omega_0}}''$ oscillate at $2\omega_0$.

III. DYNAMIC MODEL

The LTP instrument will react to the injection of the aforementioned forces and torques inflicted upon the test masses. This will result in specific kinematic excursions in both test masses. These kinematic excursions will depend on the instrument dynamics and will be sensed by the onboard interferometer. The LTP is a very complex instrument and its modeling has been presented in several references [7–9]. It can be modeled by splitting it in four main subsystems which are:

1. The dynamical model (**D**) represents the evolution of the kinematic excursions of the two test masses placed inside the LTP and the kinematics of the spacecraft. This model takes into account the coupling of the motion of each of the test masses with the motion of the spacecraft and outputs the evolution of the 15 degrees of freedom of the instrument (6 for each of the test masses and 3 more for the spacecraft).

2. The sensing mechanisms (**S**) onboard LPF are the star tracker, the inertial sensors, and the interferometer. Of special interest is the interferometer, which measures the distance between test mass 1 and the spacecraft and between the two test masses [10].
3. The controller blocks (**C**) are in charge of calculating the appropriate commands to correct the positions of the test masses and the attitude of the spacecraft. In science mode, there are two main control loops applied by the instrument. The first one — the drag free loop — takes the absolute measurement of the distance between test mass 1 and the spacecraft as a reference. It then calculates which forces should be applied to the spacecraft in order to counteract all disturbances and recreate a drag free environment for test mass 1. The second loop — the low frequency loop — takes as a reference the differential measurement between both test masses and acts on the second test mass to avoid its collision with the spacecraft walls [7]. The controllers have been designed to deliver very sensitive readings of the differential motion of both test masses between 1 mHz and 30 mHz, the measurement bandwidth of the LPF mission [2]. These two control loops are implemented inside the onboard computer of the LPF.

4. The actuators (**A**) are the physical systems that apply these commands to the test masses and to the spacecraft. The two actuator mechanisms existing in LPF are the satellite micropropulsion system, which is composed by 12 micro-newton FEEP thrusters (Field Emission Electric Propulsion), and the capacitive actuators which consist of a set of electrodes that surround the test masses and exert controlled forces on them.

This subsystem division is schematically shown in the block diagram of Fig. 2. For more detailed information of the system, the reader is referred to Refs. [7–9].

In the magnetic experiment the input signals are the magnetic forces and torques (\mathbf{f}_{mag}), and the outputs are the readings of the interferometer (\mathbf{o}). Therefore, using the block diagram scheme shown in Fig. (2), we calculate the transfer function, which results in:

$$\mathbf{o} = \mathbf{H} \cdot \mathbf{f}_{\text{mag}} \quad (16)$$

where

$$\mathbf{H} = \frac{\mathbf{D}^{-1} \cdot \mathbf{S}}{1 + \mathbf{D}^{-1} \cdot \mathbf{S} \cdot \mathbf{A} \cdot \mathbf{C}} \quad (17)$$

This transfer function depends on all the above described subsystems and represents the dynamical response of the instrument to the specific injected signals.

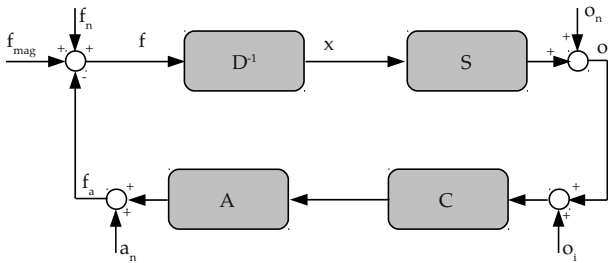


FIG. 2: Control system architecture of LISA Pathfinder. **D** stands for the dynamical matrix, **S** represents the sensing matrix of the interferometer, i.e. the matrix translating the position of the test mass, \mathbf{x} , into the interferometer readout, \mathbf{o} (\mathbf{o}_n stands for the readout noise). **A** represents the physics of the FEED and the electrostatic actuators, and finally **C**, is the controller matrix, implementing the drag free and low-frequency control loops. \mathbf{o}_i represents the displacement guidance signals. \mathbf{a}_n are the actuators noise and \mathbf{f}_a are the output forces and torques of the actuators. \mathbf{f}_{mag} are the magnetic forces and torques induced by the coils and \mathbf{f}_n are the environment force and torque noises disturbing the spacecraft.

IV. ESTIMATION MODEL

The estimation of the magnetic characteristics is performed processing the interferometer readings. To do so, we use the displacement of the differential channel ($o_{x_{12}}$), the rotation about the y -axis (o_{η_1}) and the rotation about the z -axis (o_{ϕ_1}). If cross talks are disregarded, the reading of the displacement channel stems only by the effect of the magnetic force acting along the x -axis, F_x . Analogously, something similar occurs for the two torques in each of their respective axis. Thus, we can write:

$$\begin{aligned} o_{x_{12}} &= M_x d_{x_{1\omega_0}} + \chi_o d_{x_{2\omega_0}} + \chi_e d''_{x_{2\omega_0}} \\ o_{\eta_1} &= M_z r_{y_{1\omega_0}} \\ o_{\phi_1} &= M_y r_{z_{1\omega_0}} \end{aligned} \quad (18)$$

where $d_{x_{1\omega_0}}$, $d_{x_{2\omega_0}}$ and $d''_{x_{2\omega_0}}$ are the respective transformations from force to displacement of the signals $f_{x_{1\omega_0}}$, $f_{x_{2\omega_0}}$ and $f''_{x_{2\omega_0}}$ in Eq. (15), and analogously for $r_{y_{1\omega_0}}$ and $r_{z_{1\omega_0}}$ for the case of $n_{y_{1\omega_0}}$ and $n_{z_{1\omega_0}}$. Nevertheless, because of the high complexity of the LTP instrument, this model is not sufficiently realistic. In particular, it turns out that the cross-talks cause important biases in the parameter estimates. This is because the effect of the x -force in the rotation readings and the effect of the torques in the x -axis readings are not negligible. As a consequence, we used the full three-dimensional model of the experiment:

$$\begin{pmatrix} o_{x_{12}} \\ o_{\eta_1} \\ o_{\phi_1} \end{pmatrix} = \begin{pmatrix} H_{F_x \rightarrow x_{12}} & H_{N_y \rightarrow x_{12}} & H_{N_z \rightarrow x_{12}} \\ H_{F_x \rightarrow \eta_1} & H_{N_y \rightarrow \eta_1} & H_{N_z \rightarrow \eta_1} \\ H_{F_x \rightarrow \phi_1} & H_{N_y \rightarrow \phi_1} & H_{N_z \rightarrow \phi_1} \end{pmatrix} \begin{pmatrix} f_{x_{1\omega_0}} \\ f_{x_{2\omega_0}} \\ f''_{x_{2\omega_0}} \\ n_{y_{1\omega_0}} \\ n_{z_{1\omega_0}} \end{pmatrix} \quad (19)$$

$$\begin{pmatrix} M_x & \chi_o & \chi_e & 0 & 0 \\ 0 & 0 & 0 & M_z & 0 \\ 0 & 0 & 0 & 0 & M_y \end{pmatrix}$$

where the 3×3 matrix **H** is the transformation matrix from force/torque to displacement/rotation that represents the closed loop dynamics of the instrument — see Eq. (17). This matrix is not diagonal, as it is assumed in the model in which the cross-talks are neglected — namely, Eq. (18). For instance, the effect of the torque about the y -axis and the z -axis on the $o_{x_{12}}$ displacement channel is relevant, and thus non-zero transfer functions $H_{N_y \rightarrow x_{12}}$ and $H_{N_z \rightarrow x_{12}}$ need to be considered. Hence, to estimate M_x , M_y , M_z , χ_o and χ_e , these transfer functions have to be known. This model is still a simplification, because we do not include all the degrees of freedom, but it is certainly more realistic than that of Eq. (18), which is strictly one-dimensional.

A. Estimation procedure and bias correction

The estimation procedure has been already described in Ref. [5]. However, in this paper we present an important modification to correct for the biases introduced by cross-talks. The full three-dimensional estimation model given by Eq. (19) may be regrouped as:

$$\begin{aligned} o_{x_{12}} &= (M_x + \alpha_{12}M_z + \alpha_{13}M_y) d_{x_{1\omega_0}} + \\ &+ \chi_o d_{x_{2\omega_0}} + \chi_e d''_{x_{2\omega_0}} \\ o_{\eta} &= (\alpha_{21}M_x + M_z + \alpha_{23}M_y) r_{y_{1\omega_0}} \\ o_{\phi} &= (\alpha_{31}M_x + \alpha_{32}M_z + M_y) r_{z_{1\omega_0}} \end{aligned} \quad (20)$$

where α are the cross-talks of the system (the matrix elements of **H** evaluated at the excitation frequency). If we introduce primed quantities M'_x , M'_y , and M'_z , then Eq. (20) can be written as:

$$\begin{aligned} o_{x_{12}} &= M'_x d_{x_{1\omega_0}} + \chi_o d_{x_{2\omega_0}} + \chi_e d''_{x_{2\omega_0}} \\ o_{\eta} &= M'_z r_{y_{1\omega_0}} \\ o_{\phi} &= M'_y r_{z_{1\omega_0}} \end{aligned} \quad (21)$$

and we estimate the values of \hat{M}'_x , \hat{M}'_y , \hat{M}'_z , $\hat{\chi}_o$ and $\hat{\chi}_e$ applying standard single output least square techniques [5, 16]. These values of \hat{M}'_x , \hat{M}'_y and \hat{M}'_z are biased, and do not correspond to the true magnetic moment components, M_x , M_y and M_z . Nevertheless, these biases can be corrected because we know the relation between them:

$$\begin{pmatrix} \hat{M}_x \\ \hat{M}_z \\ \hat{M}_y \end{pmatrix} = \begin{pmatrix} 1 & \alpha_{12} & \alpha_{13} \\ \alpha_{21} & 1 & \alpha_{23} \\ \alpha_{31} & \alpha_{32} & 1 \end{pmatrix}^{-1} \begin{pmatrix} \hat{M}'_x \\ \hat{M}'_z \\ \hat{M}'_y \end{pmatrix} \quad (22)$$

Note that Eq. (19) provides the values of the elements of this matrix, and that the matrix is invertible. Additionally, it is worth emphasizing that we only correct the components of the magnetic moment and no correction is considered for the susceptibility (χ_o and χ_e). This is because the magnetic susceptibility is not affected by any cross-talk. It turns out that the previously outlined procedure corrects biases of around 1% in each of the magnetic parameters, which are sizable. Finally, we also mention that during the lifetime of the mission some of the telemetry channels may fail. Thus, it is important to know beforehand that single channel estimation is still possible and that it introduces biases of $\sim 1\%$. On the other hand, by direct usage of the LTPDA toolbox, and in order to avoid additional estimation biases induced by the low frequency behavior of the instrument, we whiten the data and we eliminate its transients. These techniques are expected to be used in other experiments of the mission and are described in detail elsewhere [8, 12–14].

V. AN ANALYSIS OF THE UNCERTAINTIES

The Experiment Master Plan of the mission is aimed at determining the physical parameters of the instrument, characterizing in this way the matrix elements of \mathbf{H} . These transfer functions depend on several physical parameters. Amongst them we mention the stiffnesses of the test masses (ω_1 and ω_2 , where the subindexes 1 and 2 refer, respectively, to test mass 1 and 2), the actuator gains (namely, the gain of the FEED actuator, G_{FEED} , and that of the capacitive actuator, G_{CA}), and the interferometer cross-coupling (δ_{12}). In the end, this results in a complete characterization of the main four blocks of the instrument. Detailed information on the Experiment Master Plan and on the accuracy of the estimates can be found in Refs. [8, 11, 12].

Nevertheless, for the calculations presented here it is important to realize that some of the parameters of the model may be poorly determined or have sizable uncertainties. Therefore, in our analysis we introduce uncertainties in each of the most relevant parameters of the mission. These uncertainties are represented as b , and the subscript “NOM” stands for the nominal value of the parameter:

$$\begin{aligned} \omega_1 &= \omega_{1\text{NOM}}(1 \pm b_{\omega_1}) \\ \omega_2 &= \omega_{2\text{NOM}}(1 \pm b_{\omega_2}) \\ \delta_{12} &= \delta_{12\text{NOM}}(1 \pm b_{\delta_{12}}) \\ G_{\text{FEED}} &= G_{\text{FEEDNOM}}(1 \pm b_{G_{\text{FEED}}}) \\ G_{\text{CA}} &= G_{\text{CANOM}}(1 \pm b_{G_{\text{CA}}}) \end{aligned}$$

Clearly, the effects of these uncertainties on the estimation of the magnetic parameters need to be assessed. To this end, for each of the nine transfer functions of \mathbf{H} , we have computed the effect of the uncertainties on each of the parameters of the system. We have done this analysis for values of b ranging from -0.2 to 0.2 , and we have studied their effect on the modulus and on the phase of the transfer functions. We have found that the uncertainty on the capacitive actuator gain ($b_{G_{\text{CA}}}$) is the only one that has a relevant impact, whilst the uncertainties on the other parameters have a negligible effect.

A. The gain of the capacitive actuator

In this section we analyze the effect of the uncertainty of the capacitive actuator gain ($b_{G_{\text{CA}}}$). To this end, for a specific value of $b_{G_{\text{CA}}}$, we compute the absolute error of the modulus (\mathbf{H}_e^b) of the system transfer functions and the phase differences (\mathbf{H}_ψ^b) across the measurement bandwidth (1 mHz to 30 mHz):

$$\mathbf{H}_e^b = |\mathbf{H}^b| - |\mathbf{H}| \quad (23)$$

$$\mathbf{H}_\psi^b = \angle \mathbf{H}^b - \angle \mathbf{H} \quad (24)$$

where \angle stands for the matrix operator that calculates the phase of each of the elements of the matrix. In these expressions, the superscript “b” indicates that the specific transfer function has been calculated with a non-zero value of the parameter uncertainty. On the contrary, functions without superscript have been calculated with the nominal values of all the system parameters. Therefore, \mathbf{H}_e^b calculates the absolute error of the modulus of each of the nine functions with respect to its nominal value for one specific value of uncertainty (b), and \mathbf{H}_ψ^b gives account for their phase differences. These two matrices give a quantitative assessment of the error of the model due to the uncertainties across the entire measurement bandwidth. Moreover, the most relevant contribution in the error of the model will be due to the error in the diagonal terms of the matrix. Therefore, we analyze mainly the effects on $H_{F_x \rightarrow x_{12}}$, $H_{N_y \rightarrow \eta_1}$ and $H_{N_z \rightarrow \phi_1}$.

Fig. 3 displays the results of this sensitivity analysis for $H_{F_x \rightarrow x_{12}}$, i.e the first element of matrices \mathbf{H}_e^b and \mathbf{H}_ψ^b for several values of the uncertainty in the capacitive actuator gains, ranging from -0.2 to 0.2 . The behavior as a function of the frequency of the other two elements of the diagonal are very similar. In the top panel of this figure

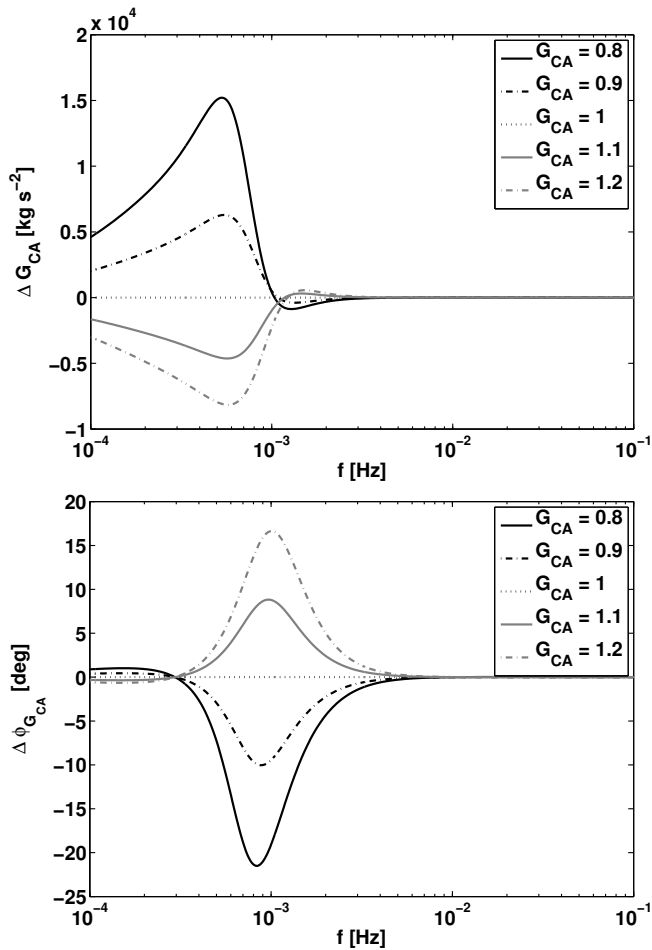


FIG. 3: Top panel: error of the modulus of the transfer function $H_{F_x \rightarrow x_{12}}^b$ with respect to its nominal behavior. This frequency-dependent relative error is plotted for different capacitive actuator gain uncertainties ranging from -0.2 to 0.2 . Bottom panel: phase differences in the $H_{F_x \rightarrow x_{12}}^b$ transfer function for different uncertainties of the gain of the capacitive actuator. The phase differences are also calculated for different relative gain uncertainties ranging from -0.2 to 0.2 .

it can be seen that the error of the modulus is especially relevant below 1 mHz, where the differences in amplitude increase up to 48% for 0.6 mHz, when the capacitive gain is 0.8 (instead of 1). The changes in modulus are also relevant between 1 mHz and 7 mHz. In the bottom panel, we examine the differences in the phase of the same transfer functions. It can be seen that there exist phase shifts of 15° for a capacitive actuator gain of 1.2 at a frequency of 1 mHz. These phase shifts are relevant between 0.4 mHz and 4 mHz. Such differences produce important biases in the estimates of the magnetic parameters. Moreover, the effect depends on the excitation frequency. Thus, the choice of the right excitation frequency (ω_0) is a crucial aspect in the experiment design. We postpone this analysis to Sect. VI, where we will study which is the optimal excitation frequency. Finally, we also mention that similar analyses for the rest of the uncertainties on the

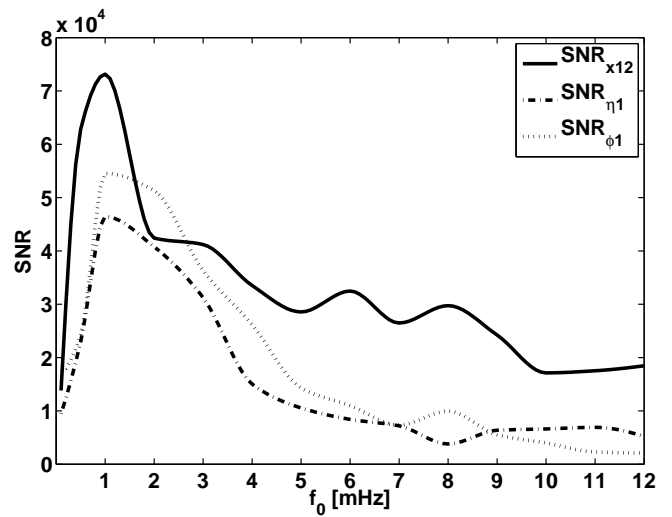


FIG. 4: Signal-to-noise ratio as a function of frequency for each of the relevant signals of the magnetic experiment, the differential channel, x_{12} — solid line — the rotation about the y -axis, η_1 — dashed-dotted line — and the rotation about the z -axis, ϕ_1 — dotted line.

nominal parameters have been performed, but are not shown here for the sake of conciseness.

VI. THE OPTIMAL FREQUENCY

Finding the optimal frequency of the sinusoidal currents injected in the coils to obtain the magnetic parameters is a crucial issue of the experiment. Actually, as it will be shown below, the optimal frequency can be obtained from a trade-off between the frequency range where the instrument presents a maximum of the signal-to-noise ratio (SNR) and the frequency range where the instrument is less sensitive to the uncertainties of the capacitive actuator gain — see Sect V A.

The SNR across the instrument measurement bandwidth for each of the channels — $o_{x_{12}}$, o_{η_1} , and o_{ϕ_1} — is shown in Fig. 4. The SNR reaches its maximum between 0.5 to 1.5 mHz for the displacement reading, and from 1 to 2 mHz for the rotation channels. This is the most sensitive band of the instrument. This is confirmed by inspecting Fig. 5, where we show the response of the system to the excitation by 4 different sinusoidal currents. All these sinusoidal currents have the same amplitude, 1 mA, but they oscillate respectively at 0.5 mHz, 2 mHz, 5 mHz and 9 mHz. In the top panel, we show the readings of the differential displacement channel to this set of four sinusoids. When exciting at 0.5 mHz the amplitude is ~ 40 nm, whereas at 2 mHz drops to ~ 5 nm. Finally, when the frequency is 5 mHz the amplitude of the excursion is only ~ 1 nm. This same effect is observed in the bottom panel, where we show the Fourier analysis of these time series. As can be seen, each of

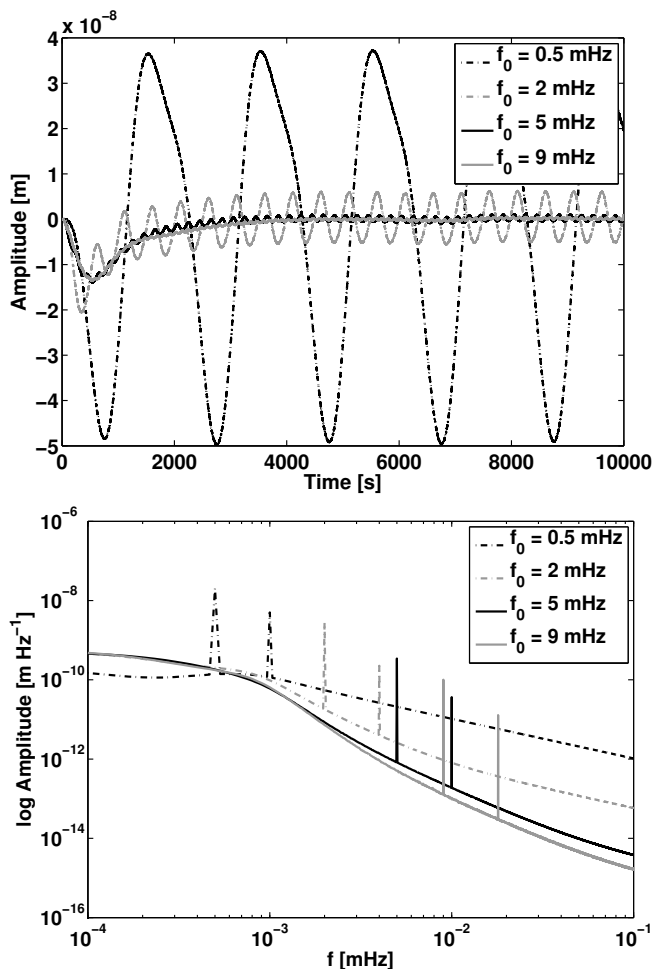


FIG. 5: Top panel: time series of the responses detected at the differential channel of the interferometer when we inject 4 different sinusoidal signals in the onboard coils. The amplitude of these sinusoids in all the cases are 1 mA and the frequencies are respectively 0.5 mHz, 2 mHz, 5 mHz and 9 mHz. Bottom panel: Fourier analysis of the time series displayed in the top panel of this figure.

the readings has a frequency component at ω_0 and a second one at $2\omega_0$, as expected. Note as well that the $2\omega_0$ components are highly attenuated with respect to the main component because they are located at higher frequencies. This simple analysis seems to indicate that the excitation frequency should be chosen around 1 mHz. However, this range of frequencies is where the uncertainty of the capacitive actuator has the largest impact on the estimates of the magnetic parameters — see Fig. 3 and section V A. Thus, the determination of the optimal excitation frequency should be the result of a joint optimization procedure, taking into account both the frequency dependence of the SNR and the uncertainties in the gain of the capacitive actuator.

To find the optimum excitation frequency we compute the estimation error of each of the magnetic parameters for different uncertainties of the gain of the capacitive

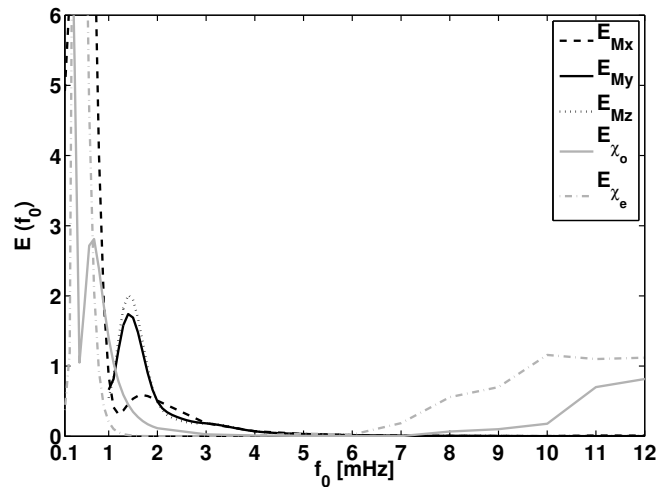


FIG. 6: Global error functions of each of the magnetic parameters with respect to the excitation frequency. The dashed black line is the global error function for M_x — that is, $E_{M_x}(f_0)$ — the black solid line is $E_{M_y}(f_0)$, and the dotted black line corresponds to $E_{M_z}(f_0)$. Finally, the solid gray line corresponds to $E_{\chi_o}(f_0)$ and the dashed gray line to $E_{\chi_e}(f_0)$.

actuator ranging from -0.2 to 0.2 . We do this for different excitation frequencies across the entire measurement bandwidth. Thus, for each magnetic parameter, we compute an error function for each gain uncertainty, $e_b(\omega_0)$. Then we add quadratically each of these functions with their appropriate weight factor:

$$E(\omega_0) = \sum_b \left(\frac{1}{b} e_b(\omega_0) \right)^2 \quad (25)$$

where b is the uncertainty in the capacitive actuator gain, in percentage. In this way we compute a global error function for each of the magnetic parameters, $E_{M_x}(\omega_0)$, $E_{M_y}(\omega_0)$, $E_{M_z}(\omega_0)$, $E_{\chi_o}(\omega_0)$, and $E_{\chi_e}(\omega_0)$. The absolute minima of these functions correspond to the best excitation frequencies for each of the parameters.

The global error functions computed in this way are shown in Fig. 6 for frequencies from 0.1 mHz to 12 mHz. For the case of remanent magnetic moment the error function presents a very broad minimum between ~ 5 mHz and ~ 11 mHz, being the absolute minimum at ~ 10 mHz. Note that at lower frequencies the global error function grows very abruptly. This occurs because, although the SNR of the experiment is larger at these frequencies, they are also very sensitive to the biases introduced by the actuator uncertainty. Note as well that the error functions have local minima at around 1 mHz, and also a local maximum between ~ 1.2 and ~ 2 mHz, following the sensitivity curve of the capacitive actuator — see Fig. 3. On the other hand, the optimal frequency needed to estimate χ_o and χ_e lies between 5 and 7 mHz. This is because these last two parameters are estimated with the $2\omega_0$ component of the x_{12} output, and higher

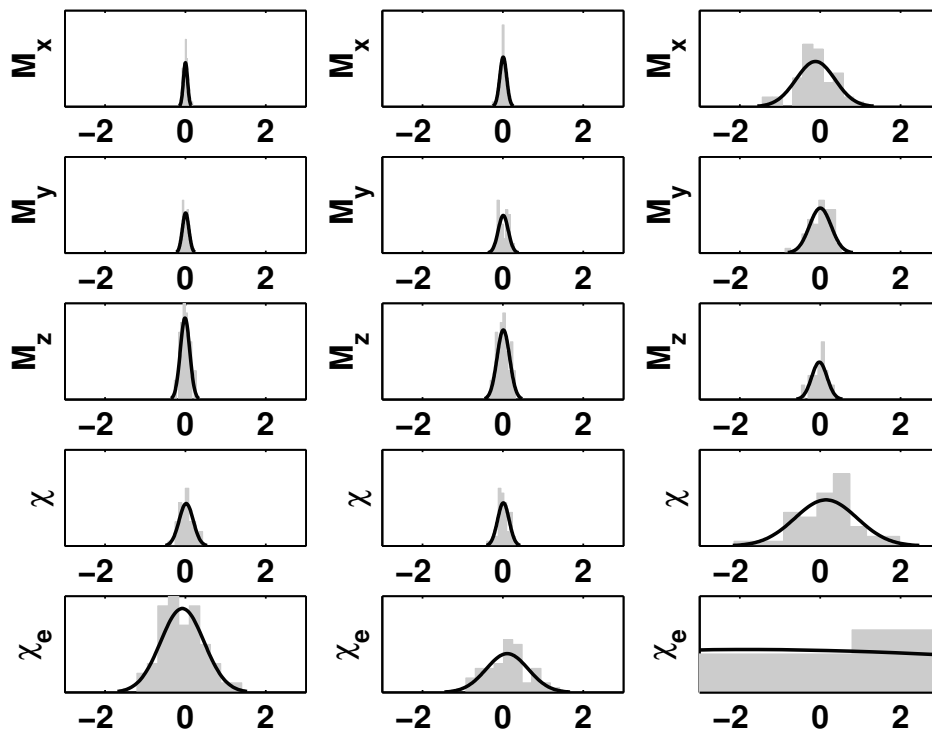


FIG. 7: Statistical distributions of the estimates for the 5 magnetic parameters of the test masses for 3 different simulations. The left column shows the statistical distribution of these parameters when the capacitive actuator gain has no uncertainty. This simulation is done for an excitation frequency of 5 mHz. The second column shows the results when the uncertainties of the capacitive actuator gains of the principal axes are modeled with a normal distribution of zero mean and 0.01 standard deviation. This simulation is done for an excitation frequency of 5 mHz, too. Finally, the third column, shows the parameter estimation results for the same experiment as in the second column, but for 1 mHz. The x -axis of each subplot shows the relative error in the parameter (in percentage).

frequencies are penalized by the larger attenuation on this frequency component. Finally, it is worth mentioning that the phase shift shown in Fig. 3 around 1 mHz penalizes the estimation at low frequencies, because the components at $2\omega_0$ suffer a different and unknown shift with respect to the ω_0 component. In summary, the best choice of excitation frequency is 5 mHz to estimate χ_o and χ_e and 10 mHz to estimate the three components of the magnetic moment. Nevertheless, if only one inflight experiment could be performed due to planning restrictions of the mission, the best frequency would be 5 mHz. This value is the result of minimizing the quadratic sum of the five error functions of the five parameters.

VII. ROBUSTNESS OF THE ESTIMATES

Finally, to conclude with our analysis we have studied the robustness of our findings. Specifically, we have tested the performance of our estimation algorithm under several circumstances. In order to model statistically its performance, we have estimated the magnetic parameters for 50 different simulated experiments and calculated the statistical distribution of the relative errors of each parameter. For example, for the case of M_x the relative

error is computed as:

$$e_{M_x} = \frac{(\hat{M}_x - M_x)}{M_x} \quad (26)$$

where \hat{M}_x is the estimated parameter and M_x represents its true value.

Here we present the results of three different simulations. In the first simulation we excite the coils with a 5 mHz sinusoid and we consider that the gain of the capacitive actuator is the nominal one. In the second simulation we maintain the 5 mHz excitation frequency, but in this case the gains of the capacitive actuators of the three main axis are modeled with a normal random distribution of zero mean and of 0.01 standard deviation. Finally, the third simulation is only performed for illustrative purposes. We maintain a random distribution of the uncertainty of the gain of the capacitive actuator, but we excite the coils at 1 mHz. Note that the analysis previously explained in Sect. IV concluded that this frequency should not be used. Consequently, this case clearly illustrates the effect of choosing a wrong excitation frequency.

The error distributions for each of the simulations previously described and for each of the magnetic parame-

TABLE I: Standard deviations of the estimated parameters for different estimation scenarios. For each of the different scenarios we calculate the ratio between the actual performance and the optimal Cramér Rao lower bound.

Run		$\Delta\hat{M}_x$	$\Delta\hat{M}_y$	$\Delta\hat{M}_z$	$\Delta\hat{\chi}_o$	$\Delta\hat{\chi}_e$
	CR bound	0.019%	0.046%	0.139%	0.083%	0.263%
1	σ	0.028%	0.067%	0.156%	0.084%	0.557%
	CR ratio	1.47	1.45	1.12	1.01	2.11
2	σ	0.123%	0.132%	0.162%	0.176%	0.632%
	CR ratio	6.47	2.86	1.17	2.12	2.40
3	σ	0.331%	0.215%	0.445%	0.553%	6.557%
	CR ratio	17.42	4.67	3.20	6.66	24.93

ters are displayed in Fig. 7, and their respective standard deviations are listed in Table I. For consistency, these results are checked against the Cramér-Rao lower bound, which gives a lower limit for the variance of the estimated parameters [16]. The Cramér-Rao bounds for each of the estimates of the magnetic parameters are listed the first row of Table I. Moreover, for each of the simulations presented here we also compute the ratio of the standard deviation to the Cramér Rao lower bound. For the first simulation we obtain variances close to the Cramér-Rao lower bound, as expected due to the large SNR. In the second numerical experiment we obtain standard deviations smaller than 0.18% for all the magnetic parameters, except for χ_e , which is the one with the lowest SNR. In this experiment, we are still close to the optimal Cramér Rao bound because we minimize the effect of the capacitive actuator uncertainty. Finally for the third simulation we obtain an important degradation of the performance of the parameter estimation procedure. In particular, the standard deviations are increased by more than 1 order of magnitude. The ratio with respect to the Cramér-Rao lower bound is also clearly much larger. Particularly, the performance of the estimate of χ_e is totally unacceptable for this experiment, obtaining an estimation performance 25 times worse than the optimal one. Finally, comparing the second and third columns of Fig. 7 — and the second and third sections of Table I — we confirm that our estimation procedure delivers better results (and close to optimal) for an excitation frequency of 5 mHz than for 1 mHz, which was the frequency adopted in the preliminary design of the experiment. This clearly demonstrates the importance of choosing the appropriate excitation frequency.

However, this is not the most robust estimate that can be obtained. In particular, we suggest to use a multi-frequency estimation technique, where the properties of the test masses are computed using the results obtained at different frequencies. In this way the effects of spurious or non-modeled effects at a given specific frequency can be minimized. This can be done weighting the results obtained for each of the magnetic parameters at each frequency by the inverse of the corresponding total error function given by Eq. (25). For instance, for the

x -component of the remanent magnetic moment we may write:

$$\hat{M}_x = \sum_{i=1}^N \frac{1}{E_{M_x}(\omega_i)} \hat{M}_{x\omega_i} \quad (27)$$

where N is the total number of frequencies used, ω_i is the corresponding excitation frequency, $\hat{M}_{x\omega_i}$ is the estimate of M_x at ω_i and \hat{M}_x is the final combined estimate. In this equation $E_{M_x}(\omega_i)$ are the weighting factors of Eq. (25) adequately normalized:

$$\sum_{i=1}^N \frac{1}{E_{M_x}(\omega_i)} = 1. \quad (28)$$

This estimation procedure provides an estimate of the magnetic characteristics of the test masses that takes into account all the limiting factors of the LTP instrument, and also delivers estimations which are robust to other unexpected (and not modeled) frequency dependent effects.

VIII. MAGNETIC CONTRIBUTION TO PROOF-MASS ACCELERATION NOISE

In previous sections we have shown that the magnetic properties of the test masses can be characterized in flight with accuracies below 1% for each of the parameters. The ultimate goal of measuring these properties is the determination of the magnetic contribution to the proof-mass acceleration noise. To do this, the estimated values of the magnetic field and magnetic field gradient at the positions of the test masses are needed. It has been concluded [17, 18] that, in the worst case, the magnetic field and its gradient can be estimated with an accuracy better than 10%. The spatial nonhomogeneities of the field are included in this uncertainty. Thus, an important goal consists in assessing how these uncertainties project into the precision of our estimate of the magnetic contribution to the total differential acceleration reading in LPF. Accordingly, we propagate the errors of the magnetic characteristics and the magnetic field and gradient into the calculation of the magnetic acceleration noise:

$$\sigma_{\text{total}} = \sqrt{\sum_{i=1}^N \left(\frac{\partial f}{\partial s_i} \sigma_{s_i} \right)^2}, \quad (29)$$

where f is the total magnetic contribution to the acceleration noise and s_i are the several sources of error. In our case, the total magnetic acceleration noise is the sum of the fluctuation of the magnetic field and magnetic field gradient of the spacecraft, the down converted AC magnetic fields, the interplanetary magnetic field fluctuations, and the Lorentz force contributions [19], whereas

TABLE II: Budget of the contribution of the magnetic field effects to the total acceleration noise and their uncertainties. These uncertainties are computed using the expected error of the magnetic characteristics reported in this paper and using the expected error of the magnetic field determination reported in Refs. [17, 18]

Contribution	Differential acceleration noise [$\text{m s}^{-2} \text{ Hz}^{-1/2}$]
Fluctuation of the spacecraft magnetic field	$(0.680 \pm 0.096) \times 10^{-15}$
Fluctuation of the spacecraft magnetic field gradient	$(1.097 \pm 0.108) \times 10^{-15}$
Down converted AC magnetic fields	$(1.265 \pm 0.254) \times 10^{-15}$
Interplanetary magnetic field fluctuation	$(1.701 \pm 0.241) \times 10^{-15}$
Lorentz force	$(0.013 \pm 0.001) \times 10^{-15}$
Total	$(2.775 \pm 0.425) \times 10^{-15}$
Requirement	12.0×10^{-15}

the sources of error are the uncertainties of the magnetic field and its gradient and those of the remanent magnetic moment and susceptibility of the test masses. The results obtained using Eq. (29) and the computed uncertainties are shown in Table II. The total magnetic contribution, which is $2.775 \times 10^{-15} \text{ m s}^{-2} \text{ Hz}^{-1/2}$ is determined with with an accuracy of $0.425 \times 10^{-15} \text{ m s}^{-2} \text{ Hz}^{-1/2}$. This means that the magnetic contribution to the total noise can be estimated with a fair accuracy, and therefore, can be subtracted from the main acceleration reading, with a relative error 15% across the whole LTP measurement bandwidth. This represents an enhancement of one order of magnitude with respect to previous studies.

IX. SUMMARY AND CONCLUSIONS

In this paper we have studied how the magnetic characteristics of the test masses onboard LISA Pathfinder can be determined. This is essential to estimate the magnetic noise contribution to the entire noise budget and, most importantly, to subtract this noise from the displacement reading. The estimation of M_x , M_y , M_z , χ_o and χ_e is done by injecting a controlled magnetic field at the position of the test masses. The field is generated by a sinusoidal current circulating through the two onboard induction coils placed at each side of both test masses. The induced magnetic field results in magnetic forces and torques on the test masses that excite their dynamics. We have shown that the force acting on the test masses has two frequencies, while the torques oscillate at single frequency, allowing to estimate the properties of the test masses by an adequate processing of three of the readings delivered by the interferometer. These readings are the differential displacement of both test masses ($o_{x_{12}}$), the rotation of test mass 1 about the y -axis (o_{η_1}) and that about the z -axis (o_{ϕ_1}). We have also shown that the time series received from the satellite's telemetry need to be whitened and split to minimize the low-frequency effects inherent in the operation of the instrument. This way,

the magnetic parameters can be estimated by a classical single-channel least-square technique once the effects produced by cross-talks are determined and corrected. Additionally, we have assessed the sensitivity of the estimation procedure to the uncertainty in the gain of the capacitive actuator of the instrument. This effect showed to be very relevant and, most importantly, it has been found to depend on the excitation frequency. Moreover, the SNR of the received signals also depends on the frequency of the injected signal. Accordingly, we have also presented a joint optimization analysis that takes into account these two factors, leading to the conclusion that the optimal excitation frequency for a joint experiment is 5 mHz. Performing the experiment at this frequency allows to estimate the magnetic characteristics without being affected by the likely uncertainty in the capacitive actuator gain. In this case we obtain parameter variances smaller than $\sim 0.7\%$ when the deviations of the gain of the capacitive actuator are $\sim 1\%$. Using all the previously explained steps and adopting this excitation frequency, the estimation turns out to be more accurate than that obtained using the preliminary design of the experiment, for which a frequency of 1 mHz was adopted. Moreover, we have suggested that a multi-frequency estimation technique could deliver estimates of the highest quality, enhancing the robustness of the experiment in front of non-modeled frequency-dependent effects. Finally, taking into account the aforementioned results, together with the results about magnetic field estimation presented elsewhere, we estimate that the total magnetic contribution to the proof-mass acceleration noise can be determined with a $\sim 15\%$ error level across the whole LTP frequency band.

Acknowledgments

This work was partially supported by MCINN grants ESP2007-61712 and AYA08-04211-C02-01. Part of this work was also supported by the AGAUR.

-
- [1] K. Danzmann, and A. Rüdiger, *Class. & Quantum Grav.*, **20**, 1-22 (2003).
- [2] M. Armano et al., *Class. & Quantum Grav.*, **26**, 094001 (2009).
- [3] F. Antonucci et al., *Class. & Quantum Grav.*, **28**, 094001 (2011).
- [4] J. Sanjuán et al., *Rev. of Sci. Inst.*, **79**, 084503 (2008).
- [5] M. Diaz-Aguiló, I. Mateos, J. Ramos-Castro, A. Lobo & E. García-Berro, *Aerospace Science & Technology*, submitted (2011).
- [6] J. D. Jackson, *Classical Electrodynamics*, 3rd edition (New York: John Wiley & Sons, 1999).
- [7] W. Fichter et al., *Class. & Quantum Grav.*, **22**, S139 (2005).
- [8] A. Monsky et al, *Class. & Quantum Grav.*, **26**, 094004 (2009).
- [9] M. Hewitson, A. Grynagier, M. Diaz-Aguiló *A linear MIMO model of LPF implemented in LTPDA*, S2-AEI-TN-3069. Albert Einstein Institute Hannover, (2010).
- [10] G. Heinzel et al., *Class. & Quantum Grav.*, **20**, 153 (2003).
- [11] M. Nofrarias, C. Rover, M. Hewitson, A. Monsky, G. Heinzel, K. Danzmann, L. Ferraioli, M. Hueller, and S. Vitale, *Phys. Rev. D*, **82**, 122002 (2010).
- [12] F. Antonucci et al., *Class. & Quantum Grav.*, **28**, 094006 (2011).
- [13] <http://www.lisa.aei-hannover.de/ltpda/>
- [14] M. Nofrarias, L. Ferraioli, G. Congedo, *Comparison of parameter estimates results in STOC Exercise 6*, S2-AEI-TN-3070, Albert Einstein Institute Hannover, (2011).
- [15] P. Welch, *IEEE Trans. on Audio and Electroacoustics*, **15**, 70 (1967).
- [16] J. Wolberg, *Data Analysis Using the Method of Least Squares* (Berlin: Springer Verlag, 2005).
- [17] M. Diaz-Aguiló, E. García-Berro and A. Lobo, *Class. & Quantum Grav.*, **27**, 035005 (2010).
- [18] M. Diaz-Aguiló, A. Lobo and E. García-Berro, *Exp. Astron.*, **30**, 1-21 (2011).
- [19] N. Brandt et al., *Experiment performance budget, LISA Pathfinder Project Documentation*, S2-ASD-TN-3036, Astrium GmbH. Germany (2010).